Numerical solution of the time-dependent Schrödinger equation for intermediate-energy collisions of antiprotons with hydrogen

J. C. Wells

Institute for Theoretical Atomic and Molecular Physics, Harvard-Smithsonian Center for Astrophysics, Cambridge, Massachusetts 02138

D. R. Schultz

Physics Division, Oak Ridge National Laboratory, Oak Ridge, Tennessee 37831-6373

P. Gavras and M. S. Pindzola

Department of Physics, Auburn University, Auburn, Alabama 36849

We study the behavior of ionization in intermediate-energy collisions of antiprotons with atomic hydrogen by direct solution of the time-dependent Schrödinger equation represented on a three-dimensional Cartesian lattice. Total cross sections for these processes are computed over the collision energy range of 0.2 to 500 keV from knowledge of the asymptotic state probabilities as a function of impact parameter. The computed ionization cross sections are in good agreement with results from recent experiments conducted at CERN [Phys. Rev. Lett. **74**, 4627 (1995)]. In the energy range from 0.2 to 30 keV, for which measurements are not available, our calculations are in qualitative agreement with other results based on classical-trajectory and coupled-channel methods, confirming the predicted significant difference from the analog proton-impact ionization process. This contrast with proton-hydrogen collisions is also explored qualitatively by employing a model two-dimensional space in which lattice solutions are less computationally intensive. [S1050-2947(96)08407-7]

PACS number(s): 34.50.Fa

I. INTRODUCTION

Only relatively recently have intense, well-collimated, monoenergetic beams of low- to intermediate-energy antimatter projectiles, such as positrons and antiprotons, been available for use in the study of ion-atom collisions (see reviews by Schultz *et al.* [1] and Knudsen and Reading [2]). The utility of these projectiles stems from the unique ability they give researchers to study the change in the collision dynamics and reaction probabilities when a single projectile characteristic is modified. That is, comparison of proton- and antiproton-impact collisions reflects only a change of the projectile's charge sign, whereas proton- and electron-impact comparisons display simultaneously a change of charge sign and a change in mass. Considerable insight has been derived in the last decade, for example, by comparing the ratio of double to single ionization by proton, antiproton, electron, and positron impact (see, e.g., [1–4]).

Furthermore, antiproton collisions with atomic hydrogen provide a fundamental and unique testing ground for the development of nonperturbative, quantal scattering methods. Unlike proton-hydrogen collisions where the final state consists of a superposition of amplitudes for elastic scattering, electronic excitation, ionization (including the well-known phenomena of "electron capture to the continuum"), and charge transfer to the projectile, the negatively charged projectile only leads to the first three of these, and actually excludes the electronic probability density from proximity to the projectile. This simplifies the requirements for the solution in that the electronic probability density leaving the target always contributes to the ionization process rather than also containing a projectile-centered component. The problem is well suited for a direct solution of the time-dependent

Schrödinger equation (TDSE) on a spatial lattice, where final-state probabilities are easily obtained by computing the overlap of the time-evolved wave function with a basis of target-centered states. Extension of pioneering work [5–9] on direct, lattice solutions of the Schrödinger equation for ion-atom collisions is straightforward for antiproton collisions with hydrogen. Because of its computationally demanding nature, however, lattice solutions of the Schrödinger equation in full three-dimensional space have only rarely been performed for atomic phenomena.

Prediction of the antiproton-impact ionization cross section of atomic hydrogen down to very low energies was given [10] in recent years, although long before this Fermi and Teller [11] had considered an analogous process in negative muon impact. Fermi and Teller pointed out that for negatively charged heavy particle impact of atomic hydrogen, all the electronic potential energy levels are promoted to the continuum for interparticle separations below a certain value. This radius has come to be known as the Fermi-Teller radius, R_{FT}, [12–14] and has a value of 0.639 a.u. for the antiproton-hydrogen system. The existence of this radius imposes a kind of ideal bound on the low-energy behavior of the ionization cross section. That is, since below this radius, all the electron energy levels are promoted to the continuum in an adiabatic collision, the cross section should be bounded from below by the value πR_{FT}^2. In reality, nonadiabatic couplings lead to a larger cross section, but a key point is that unlike the proton-impact case, the ionization cross section should not drop below πR_{FT}^2 at low collision velocities. In fact, at extremely low energies (e.g., less than 50 eV) protonium formation [15], i.e., the formation of a bound state of the antiproton with the proton of hydrogen, will dominate the

production of free electrons in this collision.

A description of the low-energy behavior of antiproton impact of hydrogen and of hydrogenic ions has very recently been given [16], supported in part by recent experiments at CERN [17] and Schrödinger equation. The subject of the present work is to provide a detailed description of the lattice methods used to produce those results, and to provide an expanded view of the technique.

To this end, in this paper we examine the direct numerical solution of the time-dependent Schrödinger equation for antiproton ionization of hydrogen using both two- and three-dimensional (2D and 3D) spatial lattices. As was shown recently for proton collisions with hydrogen [18], a TDSE solution in 2D reflects many of the qualitative features found in full 3D calculations at significantly reduced computational expense. Besides providing physical insight by surveying the variation of the collision dynamics expected in the 3D calculations, the 2D results can be used to examine convergence rates for lattice sizes, mesh intervals, and time steps. Only in 3D, however, can we calculate the ionization cross sections needed to check previous theoretical approaches and compare with the recent experimental measurements.

The remaining sections of this paper are arranged as follows: Sections II and III contain a summary of the theoretical description of the collision and the numerical methods used to solve the time-dependent Schrödinger equation for antiproton collisions with hydrogen, the results of the 2D model are presented in Sec. IV, as are the results of the full 3D calculations in Sec. V, and a discussion of the results with a brief summary and outlook is given in Sec. VI.

II. THEORY

In our study of antiproton-hydrogen collisions at intermediate energies, we use the semiclassical approximation in which the projectile travels along a well-defined trajectory in interacting with the target atom. For projectile kinetic energies of 1 keV or greater, we consider only constant-velocity, straight-line trajectories for the projectile. For the lowest-energy calculation performed (0.2 keV) in three dimensions, we numerically computed the trajectory for the projectile by solving Hamilton's equations for the antiproton moving in the adiabatic ground-state potential-energy curve of the antiproton-hydrogen system. In terms of three-dimensional Cartesian coordinates, we define the reaction to occur in the x-y plane with the beam directed along $\hat{x}$ and the impact parameter b along $\hat{y}$ defining the straight-line trajectory to be $\vec{r}_p(t) = (v_p t, b, 0)$, $t \in [-\infty, \infty]$, where v_p is the projectile's velocity. In practice, we initiate the collision with the antiproton at a finite distance away from the hydrogen atom. Except where noted, we employ atomic units in this paper (i.e., $\hbar = e = m_e = 1$).

For the energies considered here, the dynamics of an antiproton colliding with the hydrogen atom are well described by the single-particle Schrödinger equation for an electron interacting with the electromagnetic field created by the target nucleus and the projectile. Separating the Hamiltonian into time-independent and time-dependent parts, we write the Schrödinger equation in the rest frame of the target nucleus

$$[H_0 + V_p(\vec{r},t)]\psi(\vec{r},t) = i\frac{\partial}{\partial t}\psi(\vec{r},t), \qquad (1)$$

where $\psi(\vec{r},t)$ is the electronic wave function, $\vec{r}$ is the electronic position vector, and the static Hamiltonian, H_0, describes the motion of an electron in the Coulomb field created by the target nucleus with electric charge Z_t,

$$H_0 \equiv -\frac{1}{2}\nabla^2 - \frac{Z_t}{r}, \qquad (2)$$

and $V_p(\vec{r},t)$ is the time-dependent interaction of the electron with an external field generated by the projectile's motion

$$V_p(\vec{r},t) = -\frac{Z_p}{|\vec{r} - \vec{r}_p(t)|}. \qquad (3)$$

A. Two-dimensional model

As was demonstrated recently for proton collisions with hydrogen [18], a solution of the time-dependent Schrödinger equation in a two-dimensional space, designed to model the essential properties of the electronic wave function in 3D space, qualitatively includes many of the features found in a physical ion-atom collision. This reduction to two dimensions is useful as it enables the numerical consideration of relatively large collision ''volumes'' with greatly reduced computational expense, while still preserving the concept of an impact parameter. In constructing this model, we modify the short-range behavior of the electromagnetic interaction by choosing to use the so-called soft-core Coulomb potential, which has a long-range behavior identical to the Coulomb potential, but at small distances has a ''softer,'' nonsingular behavior similar to the field of a uniformly charged sphere. With the soft-core potential, the target and projectile interactions have the following form:

$$V_t(r) = -\frac{Z_t}{\sqrt{c + r^2}}, \qquad (4)$$

$$V_p(\vec{r},t) = -\frac{Z_p}{\sqrt{c + |\vec{r} - \vec{r}_p(t)|^2}}, \qquad (5)$$

where c is the real, positive-definite soft-core parameter. In the two-dimensional space $\vec{r} = (x,y)$, and the projectile's position vector is given by $\vec{r}_p(t) = (v_p t, b)$, $t \in [-\infty, \infty]$, describing a straight-line trajectory.

The soft-core parameter c provides the flexibility to choose a target interaction which produces approximately the same binding energy and electronic radial and momentum distributions as in the physical hydrogen atom. This is necessary since the two-dimensional Kepler problem possesses an analytic ground-state energy of -2 a.u. rather than the -0.5 a.u. binding of the physical atom. From experience [18], we choose the soft-core parameter $c = 0.63$ a.u.^{2} producing a reasonable two-dimensional model for hydrogen. In addition, the use of the soft-core potential ameliorates the difficulties associated with the representation of the singular Coulomb potential on a Cartesian grid with finite spacing.

This feature will be discussed more fully in connection with our three-dimensional calculations.

B. Three-dimensional calculations

The direct, numerical solution of the time-dependent Schrödinger equation in three-dimensional space for even one-electron ion-atom collisions is a computationally intensive task due to the number of lattice points or basis states required to provide a representation of reasonable fidelity. As will be discussed in the following section, we choose to solve Schrödinger's equation using lattice methods in Cartesian coordinates because such methods are efficient and simple. However, representing the Coulomb potential on a Cartesian grid with finite lattice spacing is difficult because of the singularity of the potential at the charged particle centers. Numerical schemes based on nonuniform or adaptive lattices exist for the solution of partial differential equations, but for simplicity we choose to use methods based on lattices with constant spacing in the present work.

We reduce the difficulties of the Coulomb singularity in 3D by utilizing the soft-core potential in our numerical calculations. Only for the Coulomb potential (i.e., $c = 0$ a.u.^{2}) does the interaction in Eq. (4) reproduce the physical value of the ground-state binding energy of the three-dimensional hydrogen atom, so the soft-core potential is introduced into the 3D calculations for reasons slightly different than in the 2D model. That is, the three-dimensional, lattice-based numerical solution of the hydrogen atom on a uniformly spaced Cartesian grid must be modified to avoid the singularity of the Coulomb potential if one desires accurate binding energies. In contrast, the soft-core parameter is introduced in the two-dimensional space to facilitate modeling 3D hydrogen. These issues will be discussed more fully in Sec. V.

III. NUMERICAL SOLUTION

We solve the time-dependent Schrödinger equation using lattice techniques to obtain a discrete representation of the wave function, i.e., $\psi(x,y,z) \rightarrow \psi(x_i, y_j, z_k)$, and all coordinate-space operators on a three-dimensional Cartesian mesh. Local operators such as potentials simply become diagonal matrices composed of their values at the lattice points, i.e., $V(x,y,z) \rightarrow V(x_i, y_j, z_k) \delta_{i,i'} \delta_{j,j'} \delta_{k,k'}$. Derivative operators, such as the kinetic energy, have lattice representations in terms of matrices, i.e., $\partial/\partial x \rightarrow D_{i,i'}^{(x)} \delta_{j,j'} \delta_{k,k'}$. All algorithms used are iterative in nature and are based on matrix-vector (i.e., Hamiltonian wave function) operations which are implemented in a simple form largely due to the separability of the kinetic-energy operator in Cartesian coordinates. We have implemented our solutions via two similar, but distinct, lattice methods using (i) a low-order, three-point finite-difference representation [19], and (ii) the high-order Fourier-collocation representation [20]. We choose these methods since the computational expense in both scales reasonably well with the number of lattice points. The finite-difference derivative operators are tridiagonal so that matrix-vector operations scale as the number of points on the grid, $N = N_x N_y N_z$. The Fourier-collocation derivatives may be represented either as full matrices or through a sequence of forward and backward fast-Fourier transform (FFT) operations. In practice, we choose the FFT implementation since the matrix-vector operations scale as $N \ln(N)$ using this efficient algorithm.

For the large three-dimensional lattice, complete diagonalization of the Hamiltonian operator to obtain the stationary states of interest is not practical. Therefore, we implement a partial eigensolution for the ground and low-lying bound excited states of the target atom. For the two-dimensional model, either partial or complete diagonalization can be performed. We have implemented two alternative methods for partial eigensolution. In one, we relax an initial function having a finite overlap with the ground state through propagation of the time-dependent Schrödinger equation in imaginary time ($t \rightarrow -i\tau$) using only the static Hamiltonian, H_0 [21]. We have also implemented the Lanczos algorithm [22] for a partial eigensolution of H_0. We obtain excited bound states with either partial eigensolution method through successive application of the algorithm while projecting out lower-energy or energy-degenerate states. We chose the initial estimate for each excited state to be the appropriate analytic state evaluated on the lattice. With this method, one can obtain the finite number of excited states supported on the lattice. We project the time-dependent wave function onto these excited states to determine impact-parameter-dependent probabilities for elastic scattering and excitation. Total ionization probabilities are computed using unitarity as

$$P_{\text{ioniz}}(t) \equiv 1 - \sum_{\beta} |\langle \chi_\beta | \psi(t) \rangle|^2, \qquad (6)$$

where $|\chi_\beta\rangle$ are the bound atomic states supported on the lattice ($n < 4$ in 3D in this work), and $|\psi(t)\rangle$ is the time-evolved electronic wave function, initially in the ground state of the target. Use of this simple unitarity approach utilizing only target-centered, bound-state wave functions is possible for antiproton projectiles since the charge transfer channel is closed, and accordingly no projectile-centered bound states are present.

The formal solution of the time-dependent Schrödinger equation for small time intervals ($\Delta t = t - t_0$) is given by

$$\psi(t) = U(t, t_0) \psi(t_0). \qquad (7)$$

A number of different methods may be employed to approximate the infinitesimal time-evolution operator $U(t, t_0)$,

$$U(t, t_0) = \exp\{-iH[\tfrac{1}{2}(t + t_0)]\Delta t\}. \qquad (8)$$

For the finite-difference representation, the exponential operator is approximated using the implicit Peaceman-Rachford algorithm [23]. This approximation is unitary and easily adapted to vectorized computer architectures, but requires matrix inversions that can be a problem for massively parallel computers. One may avoid the matrix inversion operations by choosing the explicit Richardson algorithm [24]. With the Fourier-collocation method, we approximate the exponential operator by K terms in a Taylor series expansion [22], where K is chosen at each step according to a convergence criterion on the wave function. The Taylor series is not explicitly unitary, but in practice is approximately unitary to a good precision.

As is common practice when using lattice-based methods, we add an imaginary, absorbing potential $-iW(x,y,z)$ to the full Hamiltonian to remove outgoing flux [25]. The real function $W(x,y,z)$ is nonzero only near the edge of the lattice, increasing from zero gradually to minimize reflections. Therefore, flux absorbed by the boundary is regarded as ionized since it is removed from the finite number of bound states supported on the lattice.

The discretization of functions and operators by lattice techniques introduces numerical errors which normally are made negligible as the parameters of the numerical lattice are refined, i.e., as the size of the numerical box is increased and the lattice spacing is decreased. While these convergence tests are relatively easy to complete for the two-dimensional calculations, extensive convergence tests for our three-dimensional calculations are prohibitively expensive. As a supplement therefore, we have used experience gained with the less expensive two-dimensional calculations as a guide in choosing the lattice parameters for the three-dimensional calculations. In addition, selectively comparing the results of calculations performed using both low-order and high-order methods implemented in two independent codes increased our confidence in the reliability of our results. Other measures used in accessing the accuracy of our three-dimensional calculations will be discussed in Sec. V.

IV. TWO-DIMENSIONAL CALCULATIONS

Our two-dimensional calculations have allowed us to quickly confirm the prediction that at low collision energies the probability of ionization remains roughly constant at very small impact parameter, to obtain a quick qualitative view of the electronic probability density for antiproton-hydrogen collisions, and to compare and contrast this density to that formed in proton-hydrogen collisions.

A four-frame sequence of the logarithm of the time-dependent electron probability density is shown in Fig. 1 for an antiproton collision with hydrogen in 2D. The incident energy of the antiproton is 20 keV, and a small impact parameter of $b = 0.4$ a.u. is chosen. In the plots, the target remains fixed at the origin of the coordinate system, while the projectile moves from right to left along a straight line at constant velocity, and is indicated by a solid circle. The contours at the peak are of the order 10^{-1}, while the lowest contours mapped are of the order 10^{-5}. In Fig. 1(a) the projectile has already passed the target and formed a small, deep hole in the electron density. The exclusion of flux from an almost circular region around the projectile is seen to persist through Figs. 1(b) and 1(c). By the time represented by Fig. 1(d), the absorbing potential at the grid boundary has eliminated reflections of the density leaving the region bounded by the extent of the numerical lattice. We note that the impact parameter is along the positive y axis and that the electronic density develops a counterclockwise rotation by the later time slices. Both this behavior and the formation of the void of density clearly come about due to the repulsion of the electronic density by the antiproton.

As a test of our procedures, we have also computed the elastic and inelastic scattering probabilities for our 2D collisions by projecting the time-evolved wave function onto the ground state of the target hydrogen atom. The first indication

that we found confirming that the ionization probability would remain high at small impact parameters, where the molecular-orbital energy curves closely approach the continuum, came from observing the total inelastic probability as a function of the impact energy for two fixed impact parameters: one at 0.2 a.u., and the other at 1 a.u. These results are shown in Fig. 2 between 100 eV and 1 MeV. Straight-line trajectories were used even at the lowest velocities since this exercise was intended simply to reveal the trend if it were indeed present. One sees for $b = 1$ a.u. that at low energies the inelastic probability drops, but that for $b = 0.2$ a.u. it plateaus. Thus, for collisions in which the projectile does not approach the target closely, the probability of ionization drops quickly at low energies, whereas in near collisions, the probability of ionization does not drop as the collision velocity is lowered. This encouraged us to attempt the full 3D calculations described in detail below.

Also of interest is a comparison in 2D of the behavior of the probability density obtained in either antiproton or proton impact. In first-order perturbation theory (Born approximation), the ionization cross section depends only on the square of the projectile charge so that it would predict the same result for antiproton and proton impact. Many works, especially over the past decade, have shown that fuller treatments of the spectrum of electrons ejected by charged-particle impact need to treat the electron as moving in the two-center field produced by the projectile and target ions, and be explicitly dependent on their charge (see, e.g., [26] and references therein). Furthermore, the dependence of the ionization cross section when either proton- or antiproton-impact occurs was considered in detail in a number of works (see, e.g., [10,1] and references therein).

The general features of these differences can readily be seen in Fig. 3 where we display four time slices after the distance of closest approach has been obtained in 20 and 100 keV proton [Figs. 3(a) and 3(c)] and antiproton impact [Fig. 3(b) and Fig. 3(d)] of hydrogen. The low-energy proton-impact frame shows the characteristic charge transfer to the projectile, as well as the elongated electronic density roughly along the internuclear axis and centered about the midpoint between the target and projectile ions associated with the so-called saddle-point mechanism of ionization. For higher impact energy, the proton case shows reduced charge transfer and an ejected electron density centered more closely about the target, as would be expected as the perturbative regime is approached. This nearly target-centered density is, however, pulled toward the projectile due to the attractive interaction of the electron with the projectile. In contrast, for antiproton impact, the opposite sign of the projectile charge prevents charge transfer, and as we have seen in Fig. 1, excludes electronic density from its vicinity. For low incident energy, the ejected electronic density is nearly circular in shape, with a void centered about the antiproton. This difference in charge sign also leads to the formation of an ''anticusp'' in contrast to the well-known electron capture to the continuum cusp formed in proton impact (see, e.g., [27] and references therein). At higher incident energy, as in the proton case, the electronic density is primarily centered on the target, but in this instance, it manifests a shape reflecting a repulsive interaction between the electron and the projectile.
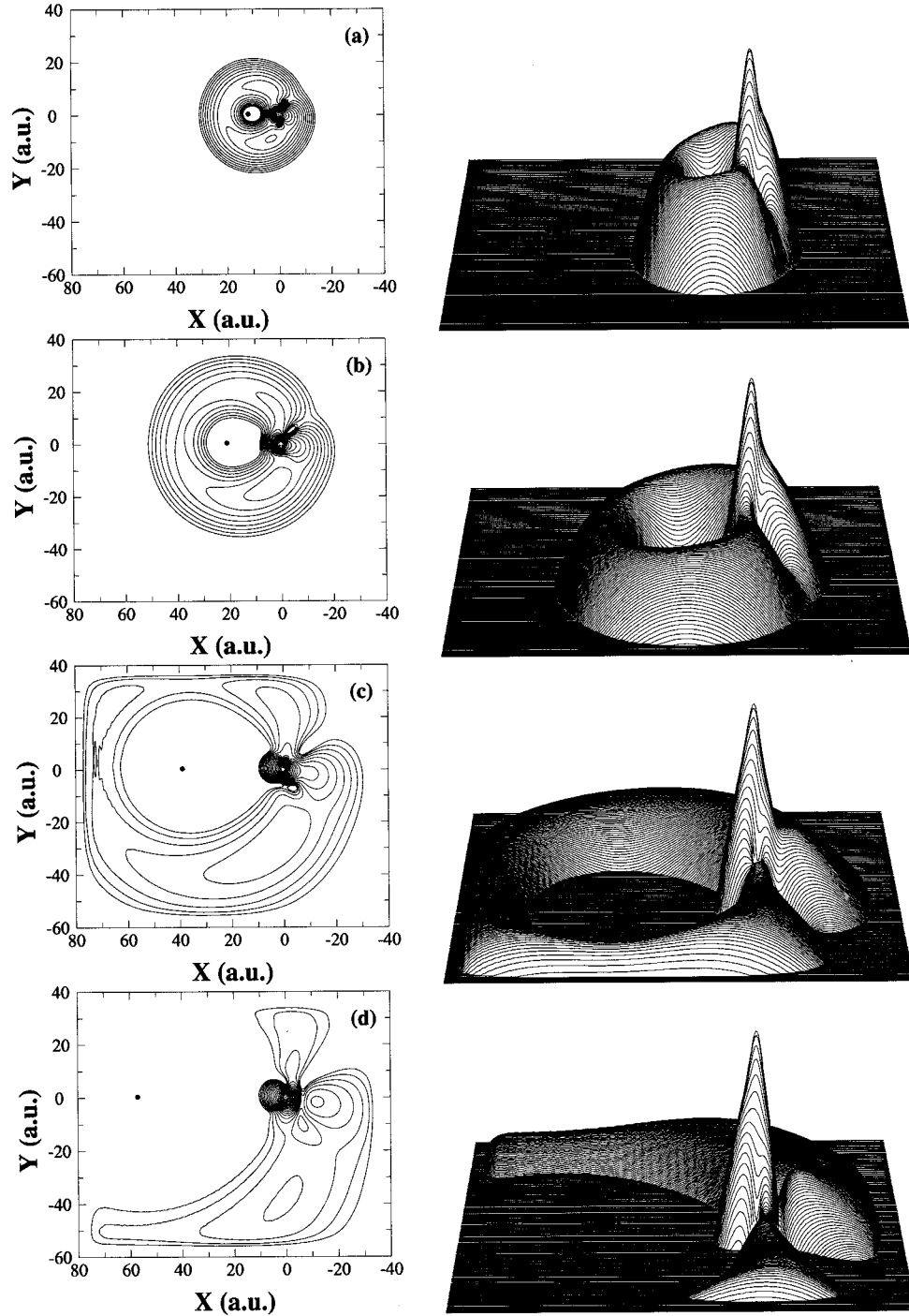
FIG. 1. The logarithm of the electronic probability density $|\psi(x,y,t)|^2$ for antiproton impact of a model hydrogen atom on a 2D Cartesian lattice at an incident energy of 20 keV and an impact parameter of 0.4 a.u. Time increases from section (a) to (d). The left column contains contours of equal probability density and the right column shows the corresponding density as a vertical displacement.

V. THREE-DIMENSIONAL CALCULATIONS

Modification of the short-range behavior of the Coulomb potential in order to improve the correspondence between the analytical solution and a numerical solution based on a relatively course grid has proved useful in other investigations [28,29]. For our purposes, we use the soft-core potential to eliminate the singularity even though, as already mentioned, any $c > 0$ implies a ground-state energy for the Schrödinger equation greater than the physical value. However, in lattice

calculations with a small soft-core parameter compared to the square of the lattice spacing h (i.e., $c \ll h^2$), the soft-core potential is not well represented near $r = 0$ in that there are too few lattice points to smoothly follow the rapid change of the V near the minimum of this function near the charge center. As a result, the numerical ground-state eigenvalue can be either smaller or larger than the analytic binding energy depending on the size of the lattice spacing and on how well the potential is represented on the lattice near its mini-
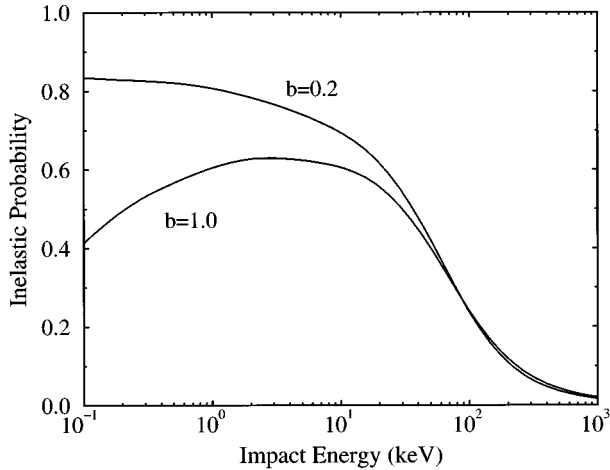
FIG. 2. The inelastic probability for antiproton impact of hydrogen in the present 2D model as a function of incident energy for impact parameters of $b = 0.2$ a.u. and $b = 1.0$ a.u.

mum. This is true because the ground state is determined by a balance between the discrete kinetic and potential energies as represented on the lattice. The lattice spacing determines the maximum kinetic energy [i.e., $T_{max} = (3\pi^2/2h^2)$]. The distance from the origin to the nearest lattice point, along with the value of c, determines to a large extent the potential energy available. Thus, for a given lattice spacing, with soft-core parameter $c \ll h^2$, one can obtain a range of ground-state energies by simply changing the position of the lattice points near $r = 0$.

Given these constraints, one can arrive at reasonable numerical approximations to the stationary states of the hydrogen atom via the following procedure. We choose to locate a lattice point at $r = 0$ so that there is a lattice point at the minimum of the soft-core potential. We choose the spatial extent of our lattice to be sufficiently large to support bound states with a principal quantum number $n < 4$. For example, a

lattice extending ± 26 a.u. in each of the three Cartesian directions is sufficient so that the value of the ground-state wave function near the boundary to be below machine precision, and the values of the $n = 2$ and $n = 3$ excited states near the boundary to be approximately 10^{-8} and 5×10^{-4}, respectively. The lattice spacing, and thus the number of points used, is constrained by the available computing resources. We have used lattices with various sizes, but our most reliable calculations were performed, for example, with 135^3 lattice points and a spacing of $h = 0.385$ a.u.

After these lattice parameters are determined, the soft-core parameter is adjusted to approximate the ground-state energy of the hydrogen atom. Using the Fourier-collocation method with the lattice parameters previously mentioned, we computed the energy of the ground state on the lattice to be $-0.499\,992$ a.u. using a soft-core parameter of $c = 0.015\,715$ a.u.^{2}. With this value of the soft-core parameter, $V_t(0) \approx -7.98$ a.u. Use of different lattice methods, e.g., finite difference methods or different lattice parameters, would require a slightly different value for the soft-core parameter to achieve the same approximation to the ground-state energy. In general, this procedure greatly reduces the dependence of our calculations on the size of the lattice spacing, since the ground-state binding energy is one of the more crucial characteristics which must be reproduced to accurately compute the ionization cross section. For reasons of consistency, we choose the soft-core parameter for the projectile interaction to be the same as that used for the target interaction.

A. Stationary-state spectrum

A quantitative method of evaluating the effect of our approximations to the stationary-state hydrogen problem is to directly compute observable quantities and compare them with analytical results. We have computed several observables, using the lattice parameters previously described, which are listed in Tables I and II. The reader will notice that
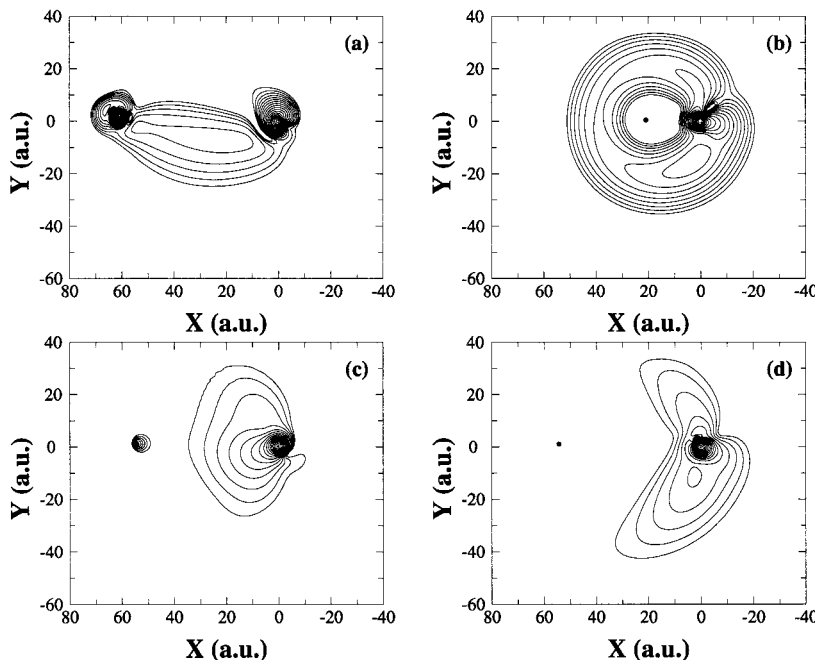
FIG. 3. The electronic probability density for proton and antiproton impact of hydrogen in the present 2D model; (a) proton impact at 20 keV and $b = 2$ a.u., (b) antiproton impact at 20 keV and $b = 0.4$ a.u., (c) proton impact at 100 keV and $b = 1$ a.u., and (d) antiproton impact at 100 keV and $b = 1$ a.u.

TABLE I. Energy expectations $\langle H_0 \rangle$, fluctuations $[\langle H_0 \rangle^2 - \langle H_0^2 \rangle]^{1/2}$, and radial expectation values $\langle r \rangle$ for the bound stationary states on a three-dimensional Cartesian lattice using the soft-core potential with $c = 0.015\,715$ a.u.^{2} and lattice spacing of $h = 0.385$ a.u.

State	$\langle H_0 \rangle$	$\sqrt{\langle H_0 \rangle^2 - \langle H_0^2 \rangle}$	$\langle r \rangle$
$1s$	-0.49999	1.9×10^{-7}	1.49
$2s$	-0.12524	8.5×10^{-7}	5.98
$2p_0$	-0.12467	9.5×10^{-7}	5.02
$2p_{+1}$	-0.12467	9.5×10^{-7}	5.02
$2p_{-1}$	-0.12467	9.5×10^{-7}	5.02
$3s$	-0.05584	4.2×10^{-6}	13.72
$3p_0$	-0.05537	4.7×10^{-6}	12.41
$3p_{+1}$	-0.05537	4.6×10^{-6}	12.41
$3p_{-1}$	-0.05537	4.6×10^{-6}	12.41
$3d_0$	-0.05561	3.6×10^{-6}	10.62
$3d_{+1}$	-0.05551	4.5×10^{-6}	10.47
$3d_{-1}$	-0.05551	4.4×10^{-6}	10.47
$3d_{+2}$	-0.05556	3.7×10^{-4}	10.54
$3d_{-2}$	-0.05556	3.9×10^{-4}	10.54

our computed observables generally correspond closely to the analytical results, but, for certain states, with only a modest degree of accuracy. Some of the error originates from the use of the soft-core potential since it breaks the $O(4)$ symmetry of the hydrogen atom, resulting in broken energy degeneracies among states with the same principal quantum number n, but differing angular momentum quantum number ℓ. Note that this error is independent of the type of lattice approximation (i.e., finite differences or Fourier collocation). The other major source of error arises since the present Cartesian lattice both formally and practically breaks the $O(3)$ rotational invariance inherent in the hydrogen atom. The modest errors resulting from this can be observed in several ways, but most clearly in the calculation of expectation values of angular momentum observables.

In Table I, we present energy expectations $\langle H_0 \rangle$, fluctuations $\eta \equiv \sqrt{\langle H_0 \rangle^2 - \langle H_0^2 \rangle}$, and radial expectation values $\langle r \rangle$ for the bound stationary states supported on our three-dimensional Cartesian lattice. The energy expectations correspond to the bound-state spectrum of hydrogen, $E_n = -(1/2n^2)$, with errors varying between 0.01% and 0.5%. The effect of broken $O(4)$ symmetry is that states with the same principal quantum number n differ in energy by approximately 0.5%. We observe effects from the broken $O(3)$ rotational symmetry in that the $3d$ states with varying magnetic quantum number are not degenerate, but differ in energy by approximately 0.2%. However, the $2p$ and $3p$ states, respectively, are degenerate to the precision of the computer. States with the same n and ℓ values, which differ only in the sign of the magnetic quantum number m, are found to be degenerate. The energy fluctuations η illustrate the effectiveness of our eigensolution algorithms discussed in Sec. III. Note that it is more difficult to obtain convergence of the iterative eigensolution for the higher-energy stationary states, and therefore they have the larger fluctuations. The computed radial expectation values are in agreement with the analytic values, $\langle r \rangle_{n\ell} = \frac{1}{2}[3n^2 - \ell(\ell+1)]$, with errors ranging between 0.3% and 1.6%.

In Table II, we present expectation values of the total angular momentum $\langle L^2 \rangle$, its z-coordinate projection $\langle L_z \rangle$, and the parity $\langle P \rangle$ for the bound stationary states supported on the lattice. The angular-momentum eigenvalues are very well reproduced for the $n=1$ and $n=2$ shells with errors occasionally as small as on the order of computer precision. The higher energy $n=3$ states are more sensitive to the box-like shape of the numerical lattice, and errors ranging between 0.1% and 1% are observed for these states. The eigenvalues of the parity operator, $P = (-1)^l$, are observed to be very well reproduced, as this symmetry is preserved in our numerical representation. In addition, we compute the expectation value $2\langle T \rangle - \langle V_t \rangle$, which is zero for stationary states of the hydrogen atom as a result of the virial theorem. The relatively small value of this quantity is further evidence

TABLE II. Expectation values of the total angular momentum $\langle L^2 \rangle$, its projection $\langle L_z \rangle$, and the parity $\langle P \rangle$ for the bound stationary states on a three-dimensional Cartesian lattice using the soft-core potential with $c = 0.015\,715$ a.u.^{2} and lattice spacing of $h = 0.385$ a.u. In addition, we compute the expectation value $2\langle T \rangle - \langle V_t \rangle$ which is zero for eigenstates of the hydrogen atom as a result of the virial theorem.

State	$\langle L^2 \rangle$	$\langle L_z \rangle$	$\langle P \rangle$	$2\langle T \rangle - \langle V_t \rangle$
$1s$	1.4×10^{-5}	1×10^{-20}	1.0000	1.9×10^{-2}
$2s$	3.3×10^{-6}	1×10^{-20}	1.0000	3.0×10^{-3}
$2p_0$	2.0000	2×10^{-21}	-1.0000	-6.6×10^{-4}
$2p_{+1}$	2.0000	1.0000	-1.0000	-6.6×10^{-4}
$2p_{-1}$	2.0000	-1.0000	-1.0000	-6.6×10^{-4}
$3s$	3.8×10^{-2}	1×10^{-16}	1.0000	-1.5×10^{-3}
$3p_0$	2.02	7×10^{-18}	-1.0000	7.8×10^{-4}
$3p_{+1}$	2.02	0.996	-1.0000	7.8×10^{-4}
$3p_{-1}$	2.02	-0.996	-1.0000	7.8×10^{-4}
$3d_0$	6.02	5×10^{-18}	1.0000	-9.5×10^{-4}
$3d_{+1}$	6.006	0.9997	1.0000	2.3×10^{-4}
$3d_{-1}$	6.006	-0.9997	1.0000	2.3×10^{-4}
$3d_{+2}$	6.013	1.9990	1.0000	-3.1×10^{-4}
$3d_{-2}$	6.013	-1.9991	1.0000	-3.0×10^{-4}
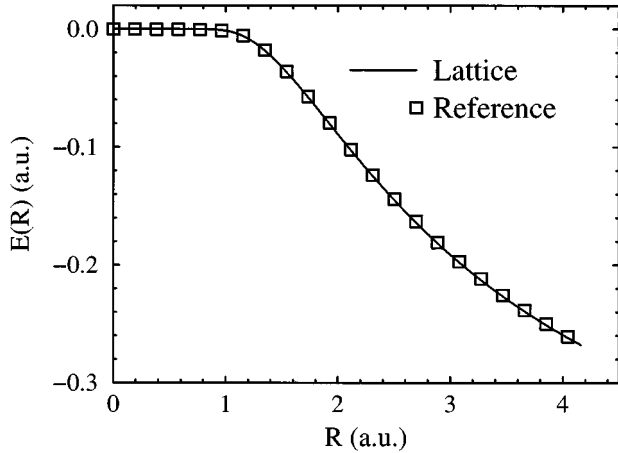
FIG. 4. The ground-state quasimolecular electronic eigenenergy for the antiproton-hydrogen system as a function of the distance (R) between the proton and the antiproton computed by solving the two-center eigenvalue problem using two independent representations: (a) a representation in Cartesian coordinates using the lattice techniques described in this paper, and (b) a representation in spheroidal coordinates in which the Hamiltonian is separable [13,16].

that we have a reasonable approximation to the bound-state spectrum of the hydrogen atom represented on a three-dimensional, uniformly-spaced Cartesian grid. We interpret the fact that the virial theorem is better approximated by the excited states, as opposed to the ground state as evidence of the poorer representation of the static potential near $r=0$. Clearly, the ground state is more sensitive to modifications in the potential near $r=0$ than are the excited states.

To further test our lattice approximations, we have computed the ground-state quasimolecular eigenenergy curve for the antiproton-hydrogen system as a function of the distance (R) between the proton and the antiproton. In Fig. 4, we plot the results of this calculation in comparison to an accurate reference solution or the ground ($1s\sigma$) energy curve [13,16]. On the linear scale presented, the agreement between these solutions is very good at all values of R. A comparison on a finer scale reveals deviations of the present lattice solution for $R<1$ a.u. originating from our present soft-core and finite lattice approaches.

A result of using the imaginary potential to eliminate unphysical reflections from the boundaries of the numerical lattice is that each stationary state wave function will possess an effective energy width (i.e., the energy will have a complex value $E+i\Gamma/2$). Therefore, probability present in any stationary state of the static Hamiltonian will decay at a constant rate in the absence of the projectile interaction. For accurate calculations of the final-state probabilities, these decay rates must be small compared to the total time used to integrate the Schrödinger equation for the collision. As a check for this effect, we have time evolved the $1s$, $2s$, and $3s$ wave functions on the lattice to ensure that the loss of probability was small and consistent with the overall accuracy for the calculation. As expected, the excited states decay more rapidly than the ground state. This observation, coupled with the observation that contributions from excitation to states with $n \geq 4$ do not significantly affect the computed ionization cross section, assured us that the choice of

box size and absorber strength was adequate for our present purposes.

B. Time-dependent solutions and total cross sections

Probabilities for inelastic scattering are obtained by projecting the time-evolved wave function onto the ground and low-lying excited states of the target atom, as described in Sec. III. By monitoring the squares of these overlaps as a function of collision time (or, equivalently, projectile position), the convergence of the probabilities to asymptotic values can be judged. Cross sections are then determined by solving the time-dependent Schrödinger equation for a range of impact parameters, b, producing the channel probabilities, $P_\alpha(b)$, and performing the integration

$$\sigma_\alpha = 2\pi \int_0^{b_{max}} b P_\alpha(b) db, \tag{9}$$

where the index α denotes the particular channel such as ionization. Approximately ten impact parameters are computed for each incident energy to assure a smooth representation of $P_\alpha(b)$. Furthermore, we have tested the dependence of the derived probabilities on such parameters as the initial and final position of the antiproton, and computed the result for a series of increasing impact parameters until the cross section is no longer sensitive to the inclusion of larger values of b.

We have estimated the accuracy of our results by comparing our Fourier collocation and finite difference results, and by testing many, but not all, of the parameters of the calculation. The primary sources of error are the finite box size and lattice spacing used for the calculations. For the lattice parameters used, we estimate that our results should have an accuracy of approximately 10%. We have already mentioned two numerical effects which cause our calculations to slightly overpredict ionization probabilities: (i) only bound states with $n<4$ are supported on the numerical lattice and, therefore, excitation to $n \geq 4$ will appear as ionization, and (ii) the stationary atomic states supported on the lattice possess a small decay rate due to the use of absorbing boundary conditions. In addition, collisional states which are populated when the projectile is near the distance of closest approach may be deformed by the presence of the finite, spatial boundary. While this error is more likely to affect the relative final-state populations of excited bound states, it also tends to increase the predicted ionization probability. The use of the soft-core potential certainly affects the small impact-parameter collisions, but, as Eq. (9) shows, these are not heavily weighted in computing cross sections.

The projection of the probability density, $\int dz |\psi(x,y,z,t)|^2$, is depicted in Fig. 5 for 20 keV antiproton impact and with an impact parameter of 0.8 a.u. In the first frame of this series of time slices, the projectile is still to the left of the target in its ground state. As the collision proceeds, the features illustrated above for the 2D model collisions are essentially reproduced, such as the roughly spherical shape to the outgoing electronic density, and the exclusion of the density from the vicinity of the projectile. Shown in Table III are the TDSE results for the $1s \rightarrow 2\ell$ excitations which compare well with previous coupled chan-
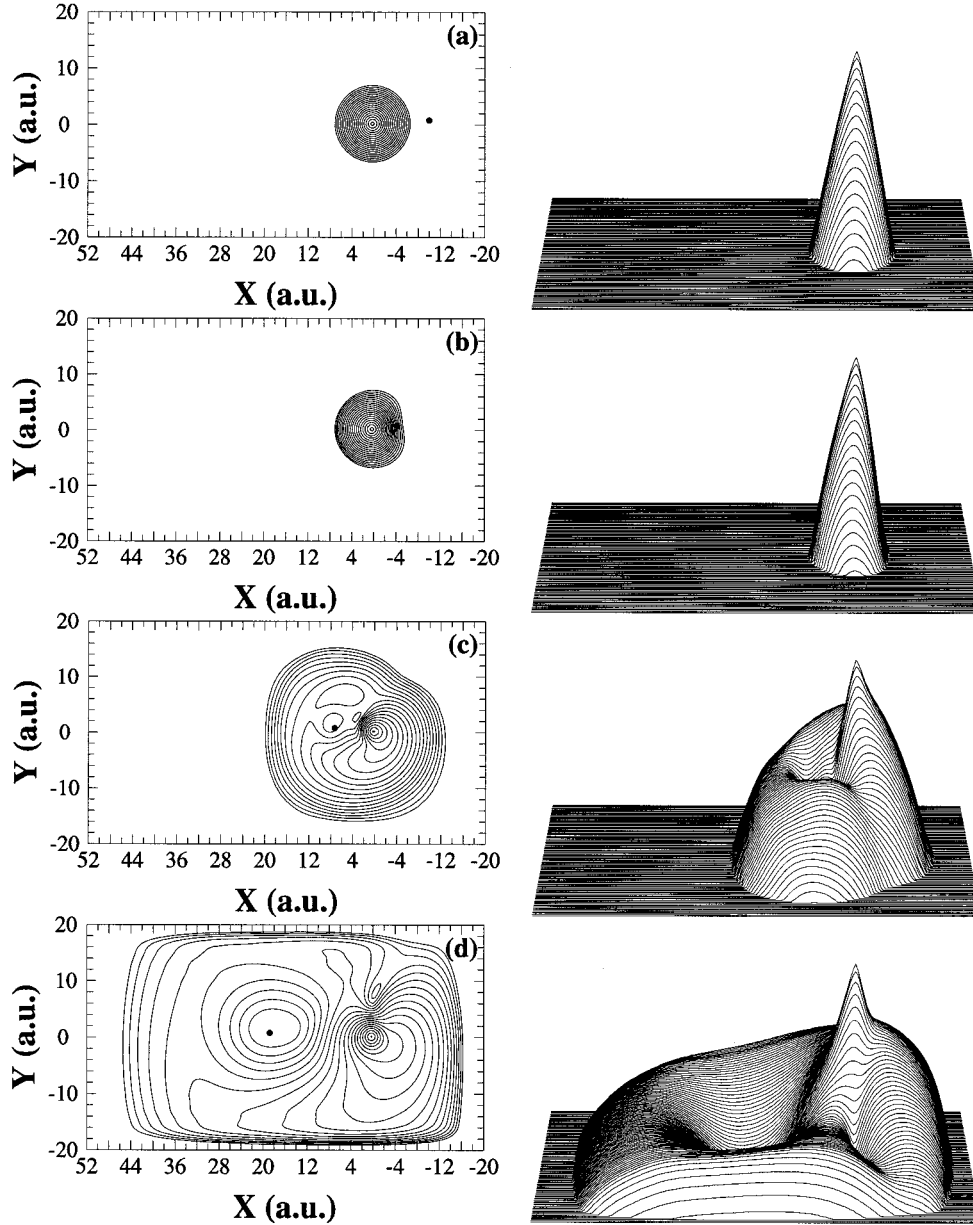
FIG. 5. The logarithm of the electronic probability density for antiproton impact of hydrogen in 3D. The incident energy is 20 keV and $b = 0.8$ a.u. Time increases from section (a) to (d). The left column contains contours of equal probability density, and the right column shows the corresponding density as a vertical displacement.

nels calculations [30] at collision energies of 30, 60, and 100 keV.

At high impact energy, where first-order perturbation theory is valid, the present ionization probability as a function of impact parameter can be directly compared with re-

sults of the Born approximation. At the highest energy considered here, this regime is almost reached. In Fig. 6 this comparison is made for an incident energy of 500 keV. The figure shows a very good agreement between the TDSE and Born approximation results [31], where we have plotted

TABLE III. Excitation cross sections for antiproton collisions with hydrogen in units of 10^{-18} cm^2.

Energy (keV)	TD method $1s \rightarrow 2s$	CC method [30] $1s \rightarrow 2s$	TD method $1s \rightarrow 2p$	CC method [30] $1s \rightarrow 2p$
30.0	6.26	7.15	70.9	79.0
60.0	5.91	5.52	78.8	82.1
100.0	4.87	4.53	70.7	75.3
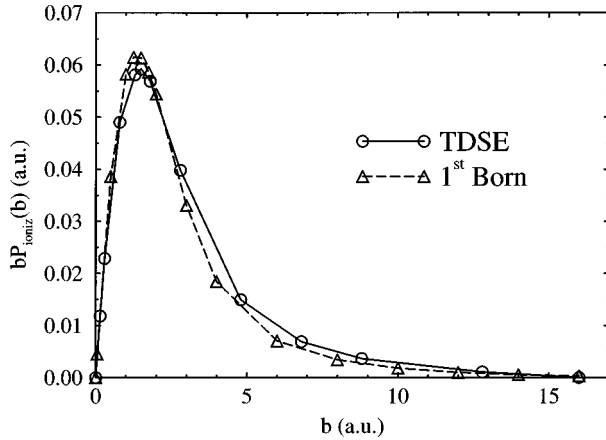
FIG. 6. Comparison of the present TDSE ionization probability as a function of impact parameter for 500 keV antiproton impact of hydrogen with results of the first-order Born approximation.

$bP(b)$ so that the area under each curve is proportional to the predicted total cross section. Differences between the two results can be attributed to inadequacies of the present lattice treatment, or to the fact that the incident energy is not quite large enough to assure the strict applicability of first-order perturbation theory. This 500 keV TDSE result agrees well also with the experimentally measured data of Knudsen [17], the atomic orbital (AO) close coupling results of Martir *et al.* [30], of Toshima [32], and of Schiwietz [33], and the two-center, first-order perturbation theory result of the continuum-distorted-wave–eikonal-initial-state (CDW EIS) approximation [16], as seen in Fig. 7.

Furthermore, Fig. 7 shows the results of TDSE calculations performed at several energies and shows that they agree well over the energy range between 30 and 100 keV with experiment, the prediction of the classical trajectory Monte Carlo (CTMC) method [10,16], and the AO results. In the energy range from 20 down to 1 keV, the TDSE calculations agree well with the AO calculations of Schiwietz [33] within the accuracy attributed to our lattice calculations, while the classical trajectory Monte Carlo method overestimates the cross section in this energy regime. We note that our calculation of the ionization cross section at 0.2 keV includes non-straight-line, nonconstant velocity trajectories as previously described. Also shown in Fig. 7 is the ideal lower bound set by the Fermi-Teller cross section πR_{FT}^2. Note that nonadiabatic effects are inferred to be relatively strong since the predicted cross sections are approximately a factor of 3 larger than πR_{FT}^2 for the lower energies considered.

Although the CDW EIS method is not applicable for low impact energies, we have included in Fig. 7 the result of this theory for comparison. The breakdown of the theory below approximately 50 keV is clearly visible. The CDW EIS cross section, as well as any result based on conventional first-order perturbation theory, will drop precipitously at low energies due to the rapidly oscillating term it contains resulting from the vanishingly small separation of the bound-state energy level from the continuum at small distances.

VI. DISCUSSION AND SUMMARY

In general, for heavy-particle collisions with an atom, when the effective collision time, b/v_p, is large compared
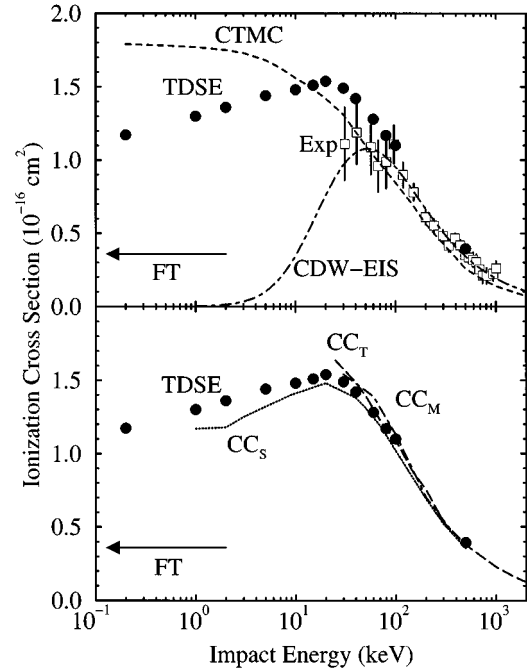
FIG. 7. The total cross section for ionization as a function of incident energy for antiproton-hydrogen collisions. The data are separated into two sections for clarity. In the top section, the open squares represent the experimental measurements of Knudsen *et al.* scaled as described in Ref. [17], the solid circles represent the present TDSE results, the dashed curve represents the classical trajectory Monte Carlo (CTMC) technique [10,16], and the dash-dot curve represents the continuum-distorted-wave–eikonal-initial-state (CDW EIS) approximation [16]. In the bottom section, the solid circles represent the present TDSE results as compared with three independent atomic-orbital close coupling results. The dash-dot curve represents the result of Martir *et al.* (CC_M [30]), the dashed curve represents the result of Toshima CC_T [32], and the dotted curve represents the result of Schiwietz CC_S [33]). Also shown in both sections is the limit given by the Fermi-Teller cross section, πR_{FT}^2, indicated by the arrow.

with the period which characterizes a transition, the colliding system may adiabatically deform during the course of the collision rendering inelastic collisions improbable. For the case of ionization in antiproton-hydrogen collisions, this means that the probability for ionization is very low for collisions in which $b/v_p \gg E(R)^{-1}$ for the ground-state electronic energy curve. While this adiabaticity condition always holds for sufficiently large impact parameters, this condition can never be satisfied for $b \lesssim R_{FT}$ since all electronic potential-energy curves are mixed with the continuum at this value of the internuclear distance. Assuming straight-line trajectories, this imposes an ideal low-energy bound on the ionization cross section of πR_{FT}^2. Intermediate to these extremes of very small and large impact parameters, we have a regime for which $R \gtrsim R_{FT}$ where the ground-state electronic energy curve approaches closely to the continuum edge, resulting in nonadiabatic transitions to be very probable in collisions for which $v_p/b \gg E(R)$. Since $R \sim b$ near the distance of closest approach, we can express this condition as $v_p \gg RE(R)$. For projectile velocities $\gtrsim 0.1$ a.u., this condition is satisfied for $R \lesssim 1$ a.u., providing a practical limit for

the low-energy ionization cross section of approximately π a.u. This practical low-energy limit for the ionization cross section is very consistent with our computed results presented in Fig. 7, and provides an explanation for our results being approximately a factor of 3 larger than πR_{FT}^2 at low energy.

From these considerations, one sees that the ionization cross section for antiproton-hydrogen collisions is dominated by nonadiabatic transitions occurring at $R > R_{FT}$ down to collision energies near the threshold for direct ionization. It has been predicted [34] that the low-energy cross section would rise as the energy decreases due to the effect of the attractive force between the projectile and target (proton) distorting trajectories with larger impact parameters to attain smaller values of R. This effect is appreciable in CTMC calculations [16] beginning at a collision energy of 0.1 keV. However, for our TDSE calculations, the minimum energy considered (0.2 keV) is not sufficient for the cross section to display this behavior. The size of the trajectory effect was briefly explored in our TDSE calculations at 0.2 keV by comparing probabilities for ionization at an impact parameter of $b = 0.6$ a.u. with and without the non-straight-line trajectories for the projectile. Inclusion of these effects in this case resulted in an increase in the calculated ionization probability of approximately 3%.

In summary, a three-dimensional lattice solution of the time-dependent Schrödinger equation has been employed to study the behavior of ionization in collisions of antiprotons with atomic hydrogen. The computational approach is found to be applicable over an extremely wide energy range, encompassing the low-energy, two-center, (nearly) molecular regime, as well as the high-energy, one-center Born limit. The collision dynamics are revealed by examination of time-evolving electron probability density plots. Furthermore,

projections of the wave function onto the stationary states of the target are used to obtain ionization cross sections in good agreement with very recent experiments and previous theoretical results. These results have confirmed the behavior predicted on the basis of the Fermi-Teller model and earlier CTMC calculations of the ionization cross section at low energy. Furthermore, these results indicate a significant nonadiabatic contribution to the ionization cross approximately modeled by the CTMC approach, well in excess of the strictly adiabatic picture of the Fermi-Teller model. In the future we plan to make 2D and 3D lattice calculations for a variety of one (active) electron collision systems. One of the strengths of a computational method based on the direct solution of the time-dependent Schrödinger equation is its straightforward application to many different types of problems in atomic physics.

[1] D.R. Schultz, R.E. Olson, and C.O. Reinhold, J. Phys. B **24**, 521 (1991).

[2] H. Knudsen and J.F. Reading, Phys. Rep. **212**, 107 (1992).

[3] L.H. Andersen, P. Hvelplund, H. Knudsen, S.P. Moller, A.H. Sorensen, K. Elsener, K.-G. Rensfelt, and E. Uggerhoj, Phys. Rev. A **36**, 3612 (1987); L.H. Andersen, P. Hvelplund, H. Knudsen, S.P. Moller, K. Elsener, K.-G. Rensfelt, and E. Uggerhoj, Phys. Rev. Lett. **57**, 2147 (1986).

[4] M. Charlton, L.H. Andersen, L. Brun-Nielsen, B.I. Deutch, P. Hvelplund, F.M. Jacobsen, H. Knudsen, G. Laricchia, M.R. Poulsen, and J.O. Pedersen, J. Phys. B **21**, L545 (1988).

[5] V. Maruhn-Rezwani, N. Grün, and W. Scheid, Phys. Rev. Lett. **43**, 512 (1979).

[6] C. Bottcher, Phys. Rev. Lett. **48**, 85 (1982).

[7] K.C. Kulander, K.R. Sandhya Devi, and S.E. Koonin, Phys. Rev. A **25**, 2968 (1982).

[8] C. Bottcher, G.J. Bottrell, and M.R. Strayer, Comput. Phys. Commun. **63**, 63 (1991).

[9] N.H. Kwong, K.J. Schaudt, and J.D. Garcia, Comput. Phys. Commun. **63**, 171 (1991).

[10] D.R. Schultz, Phys. Rev. A **40**, 2330 (1989).

[11] E. Fermi and E. Teller, Phys. Rev. **72**, 399 (1947).

[12] O.H. Crawford, Proc. Phys. Soc. London **91**, 279 (1967).

[13] I.V. Komarov, L.I. Ponamerev, and S.Yu. Slovyanov, *Spheroidal and Coulomb Spheroidal Functions* (Nauka, Moscow, 1976).

[14] M. Kimura and M. Inokuti, Phys. Rev. A **38**, 3801 (1988); I. Shimamura, *ibid.* **46**, 3776 (1992).

[15] J.S. Cohen, Phys. Rev. A **36**, 2024 (1987).

[16] D.R. Schultz, P.S. Krstić, C.O. Reinhold, and J.C. Wells, Phys. Rev. Lett. **76**, 2882 (1996).

[17] H. Knudsen, U. Mikkelsen, K. Paludan, K. Kirsebom, S.P. Moller, E. Uggerhoj, J. Slevin, M. Charlton, and E. Morenzoni, Phys. Rev. Lett. **74**, 4627 (1995).

[18] P. Gavras, M.S. Pindzola, D.R. Schultz, and J.C. Wells, Phys. Rev. A **52**, 3868 (1995).

[19] M.S. Pindzola and C. Bottcher, Laser Phys. **3**, 748 (1993).

[20] D. Kosloff and R. Kosloff, J. Chem. Phys. **52**, 35 (1983).

[21] A. Goldberg and J. L. Schwartz, J. Comput. Phys. **1**, 433 (1967); **1**, 448 (1967).

[22] J. C. Wells, A. S. Umar, V. E. Oberacker, C. Bottcher, M. R. Strayer, J. S. Wu, J. Drake, and R. Flanery, Int. J. Mod. Phys. C **4**, 459 (1993).

[23] D. W. Peaceman and H. H. Rachford, J. Soc. Indust. Appl. Math. **3**, 28 (1955).

[24] J. L. Richardson, Comput. Phys. Commun. **63**, 84 (1991).

[25] Kosloff and Kosloff, J. Comp. Phys. **63**, 363 (1986).

[26] C.O. Reinhold and R.E. Olson, Phys. Rev. A **39**, 3861 (1989).

[27] C.O. Reinhold and D.R. Schultz, Phys. Rev. A **40**, 7373 (1989).

[28] K.C. Kulander, K.J. Schafer, and J.L. Krause, in *Atoms in Intense Laser Fields*, edited by M. Gavrila (Academic Press, New York, 1992), p. 247.

[29] C. Bottcher (private communication).

[30] M. H. Martir, A. L. Ford, J. F. Reading, and R. L. Becker, J. Phys. B **15**, 1729 (1982).

[31] C.O. Reinhold (private communication).

[32] N. Toshima, Phys. Lett. A **175**, 133 (1993).

[33] G. Schiwietz (private communication); J. Phys. B **29**, 307 (1996).

[34] P.S. Krstić, D.R. Schultz, and R.K. Janev, J. Phys. B **29**, 1914 (1996); S.Yu. Ovchinnikov (private communication).